

# NATURAL LAMINAR FLOW WING DESIGN OF SUPERSONIC TRANSPORT AT HIGH REYNOLDS NUMBER CONDITION

Hiroaki ISHIKAWA\*, Naoko TOKUGAWA\*\*, Yoshine UEDA\*\*\*  
and Kenji YOSHIDA\*\*  
\*TOUA Co. Ltd., \*\*JAXA, \*\*\*Tokyo Business Service Co. Ltd.

**Keywords:** *supersonic, SST, NLF, CFD, inverse-method*

## Abstract

*A natural laminar flow wing was designed using a computational-fluid-dynamics-based inverse design method of supersonic transport at high-Reynolds number condition to reduce the friction drag of a large supersonic commercial transport. Design of the higher Reynolds number condition is more difficult than the lower Reynolds number condition because a target pressure distribution that can achieve natural laminar flow has steeper pressure gradients at the leading edge than a low Reynolds number condition. This study improved the conventional natural laminar flow design method by inverse design starting from a low-Reynolds number condition design, variable smoothing strength, the modified trailing edge closing method, and so on. The improved inverse design method was applied to a large supersonic transport with 300 passengers at the condition of Mach 2.0 and high Reynolds number of approximately 126 million based on the mean aerodynamic chord. The results and the effects of the improved natural laminar flow design are described herein.*

## 1 Introduction

Supersonic flight of future airliners offers the possibilities of meeting growing airlift demand and of liberating passengers from the inconvenience and bad health effects of long flights. An important problem is its high fuel cost. Aerodynamic drag reduction can resolve that economic hurdle. Natural laminar flow (NLF) wing design technology is an important

means to reduce the aerodynamic drag. The Japan Aerospace Exploration Agency (JAXA) developed a scaled supersonic experimental airplane called NEXST-1 in National Experimental Supersonic Transport (NEXST) project with the NLF wing design concept and verified the effects of its concept through flight testing [1,2]. Results showed some improvement of efficiency of the NLF wing design process, but underscored the necessity of its extension to a higher Reynolds ( $Re$ ) number condition of a large supersonic transport. For this study, the NLF design system was modified to achieve the NLF wing. Then this new design method was applied to the high- $Re$  number condition of a large supersonic transport (LSST).

## 2 JAXA's conceptual supersonic transport

### 2.1 NEXST-1 airplane (Low- $Re$ number)

The NEXST-1 airplane is a scaled supersonic experimental airplane with 11.5 m length and 4.72 m wingspan, as shown in Fig. 1. It has a scale ratio of 11% of a future commercial SST planned by JAXA. It has no propulsion system because NEXST-1 is a gliding experimental airplane. Four design concepts (arrow wing planform, warped wing, area-ruled fuselage and NLF wing) were applied to the NEXST-1 to reduce aerodynamic drag at a supersonic cruise condition (lift coefficient  $C_L=0.1$  corresponding to an angle of attack  $\alpha=2.0$  deg and Mach number  $M=2.0$ ). The arrow wing planform with an optimum

slenderness ratio was selected from supersonic linear theory[3] in compromising aerodynamics and structural constraints. Its aspect ratio was 2.2. The swept angle of the leading edge was 66 deg (in-board wing) and 61.2 deg (out-board wing), which were subsonic leading edges at  $M=2.0$ . To reduce the lift-dependent drag, a warped wing was designed using Carlson’s method[4]. An optimum load distribution was obtained using an optimum combination of wing camber and twist distributions. A supersonic area-ruled fuselage was also applied to reduce wave drag attributable to volume. The fuselage was designed so that the cross-sectional area distribution of the overall shape of the aircraft is the same as that of the equivalent Sears–Haack body[5]. The NLF wing design concept is based on suppression of the Tollmien–Schlichting wave instability and the cross-flow instability. To suppress both instabilities, an optimum pressure distribution was found using a practical transition prediction method with a linear stability analysis based on the  $e^N$  method [6,7]. Then the NLF wing was designed from the above pressure distribution using a computational fluid dynamics (CFD)-based inverse design method [8–10] on the expected flight test condition (altitude  $H=15$  km,  $M=2.0$ , the MAC (=2.754 m) based  $Re=22.212 \times 10^6$ ,  $C_L=0.1$ ,  $\alpha=2.0$  deg).

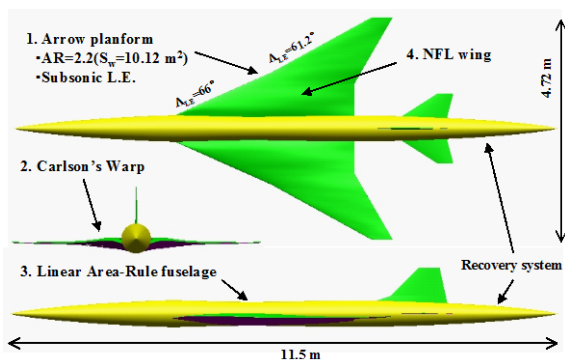


Fig 1. NEXST-1 configuration [1,2].

## 2.2 Large scale supersonic transport (LSST) (High- $Re$ number)

A large future commercial SST called LSST was planned by JAXA. The LSST has 9,000 ft<sup>2</sup> (836.07 m<sup>2</sup>) wing area, 300 ft (91.437 m) fuselage length, 140.7 ft (42.889 m) span

length, and 30,000 ft<sup>3</sup> fuselage volume with 300 passengers as shown in Fig. 2. The vertical tail planform and mounting position are similar to those of *Concorde*. The planform is the same as the NEXST-1 because the NEXST-1 airplane is an 11% scaled experimental airplane of the LSST. The Carlson’s warp wing and the area ruled fuselage are also considered at the conceptual design phase. The supersonic cruise condition corresponding to the design point is Mach number of 2.0, design  $C_L$  of 0.1,  $\alpha=2.0$  deg angle of attack, and  $H=18$  km altitude. The unit length Reynolds number,  $Re_{unit}$ , is  $5.05 \times 10^6$  1/m. The MAC (=25.037 m) based Reynolds number,  $Re_{MAC}$ , is  $126.42 \times 10^6$ , which is larger than the NEXST-1 airplane’s Reynolds number ( $22.212 \times 10^6$ ).

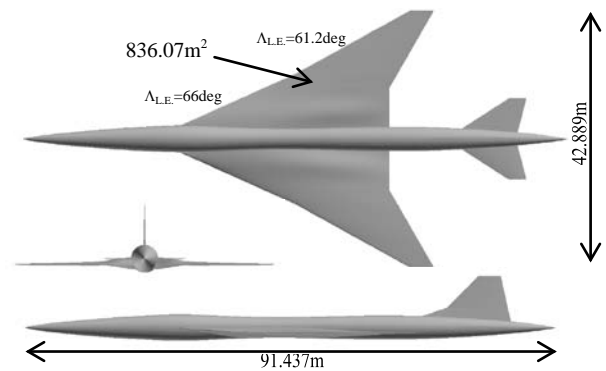


Fig 2. LSST configuration.

## 3 NLF design method

### 3.1 Fundamental design method

#### 3.1.1 Inverse design process

The supersonic NLF wing design system [10] using CFD-based inverse design method is performed according to the design process described in Fig. 3. First, the baseline configuration is determined by the other design concepts: arrow wing planform, warped wing, and area-ruled fuselage. Then the baseline configuration is smoothed if necessary. Next, the computational grid on the smoothed surface and in the space is generated for CFD analysis. Then CFD analysis is conducted to obtain the surface  $C_p$  distribution of the wing surface. The  $C_p$  distribution by CFD is compared with the

target  $C_p$  distribution, where the target  $C_p$  distributions on the upper wing surface of the baseline configuration are determined using linear stability analysis. If the  $C_p$  distribution by CFD corresponds sufficiently to the target  $C_p$  distribution, then the design process is finished. If the  $C_p$  distribution by CFD does not satisfy the convergence criteria, then the NLF wing is designed using the inverse design method. As described in this paper, determination of the target pressure distribution, the CFD analysis method, the inverse design method, and details of the design evaluation are presented in later sections.

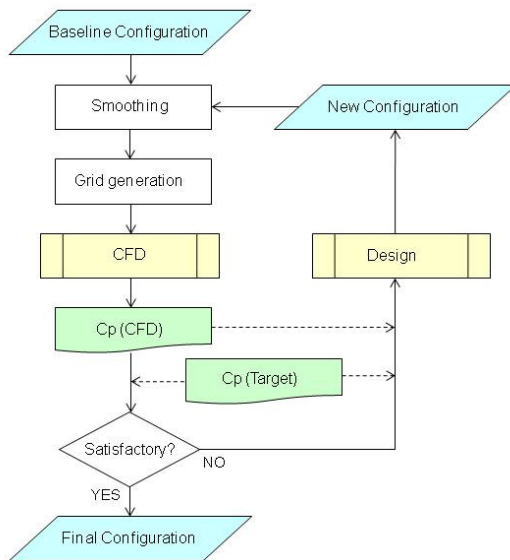


**Fig 3. Design process of the NLF wing.**

### 3.1.2 Target Pressure distributions

The target  $C_p$  distributions are obtained using two design concepts. On the upper wing surface target, the  $C_p$  distributions are determined by the NLF wing design concept [11,12]. The differential pressure distributions between the upper surface and lower surface on each wing section were obtained from Carlson's warp design [4]. Then, the lower target  $C_p$  distributions were defined by adding these differential  $C_p$  distributions to the upper distributions.

The upper wing surface target  $C_p$  distributions [11,12] were obtained using boundary layer analysis and linear stability analysis. The boundary layer profile included

density, velocity, temperature, and pressure obtained using boundary layer analysis from the arbitrary pressure distribution on the wing surface. Then linear stability analysis was conducted using LSTAB [6,7] code, which is JAXA's in-house code based on  $e^N$  method. For this target  $C_p$  distribution determination process, the  $N$  value was assumed as 14, which derives from NASA's flight test results [13]. Figure 4 presents the target  $C_p$  distributions at the in-board cross section ( $y/s=0.3$ ) and the out-board cross section ( $y/s=0.7$ ). These target pressure distributions have a sharply increased pressure gradient in the narrow region of the front part of the wing, and have gradual pressure gradients at other chord locations. Results show that discrepancies are observed between the target  $C_p$  and the baseline  $C_p$ , which corresponds to the initial shape of the NLF wing design phase. The baseline  $C_p$  distributions are expected to converge to the target  $C_p$  distributions.

The boundary layer transition on-set positions are also estimated by the transition analysis based on  $e^N$  method ( $N=14$ ). Figure 5 shows boundary layer transition analysis results from obtained target  $C_p$  distribution and the baseline configuration at  $H=18$  km altitude: the supersonic flight cruise condition. "Baseline" denotes the predicted boundary layer transition position using its  $C_p$  distributions from the CFD analysis. The baseline transitions almost around the leading edge ( $x/c=0.03-0.4$ ) ( $x_{Transition}-x_{L,E}=0.1-0.2$  m). However, the boundary layer transition position by the target  $C_p$  distributions is located in a backward region ( $x/c=0.25-1.0$ ) ( $x_{Transition}-x_{L,E}=6.7-8.7$  m). Therefore, the target  $C_p$  distributions can have NLF wing characteristics.

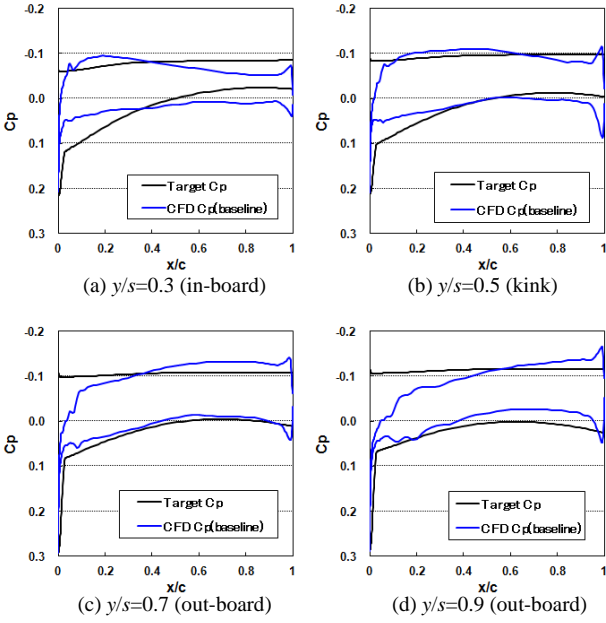


Fig 4. Target  $C_p$  distributions [12].

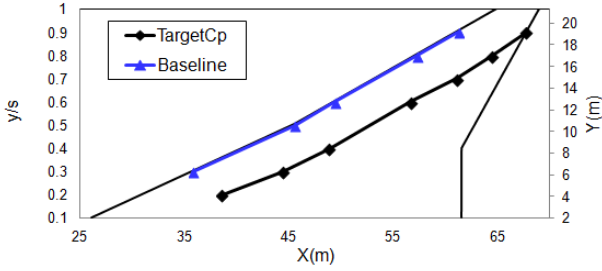


Fig 5. Estimated boundary layer transition on-set ( $N=14$ ) of the high- $Re$  condition (LSST).

### 3.1.3 Geometry smoothing and grid generation

The next-generation design shape is obtained by adding a geometrical correction function ( $\mathcal{A}f$ ) to the discrete panel of previous geometry in the inverse design process. The new design shape generally has some oscillations and discontinuities that should be removed to perform high-quality NLF design. Particularly, it is desirable to define the wing cross section geometry using a continuous function to smooth the first derivative and the second derivative of the geometry. In this study, the idea of a conformal mapping used in the fluid analysis of two-dimensional (2D) potential flow is applied to smoothing of the 2D wing cross section. Figure 6 shows the smoothing process with conformal mapping. First, the arbitrary wing cross sections with a twist angle are transformed to a physical plane with untwist and are scaled into 1.0 chord length. In this

subsection, the physical plane,  $z$ , is assumed as shown below.

$$z = x + iy. \quad (1)$$

The mapping plane,  $\zeta$  is assumed using angle variables  $\theta$  as presented below.

$$\zeta = \xi + i\eta = \cos \theta + i(\sin \theta). \quad (2)$$

The geometry in the physical plane is definable by the conformal mapping function expanded into a complex form of Fourier series using the expansion method described by Imai [14,15].

$$z = f(\zeta) = \sum_{n_c=-1}^{N_c} (P_{n_c} + iQ_{n_c}) \zeta^{n_c}. \quad (3)$$

In Eqs. (1–3), the real part shows the chord-wise direction value  $x$ . The imaginary part shows the height direction value  $y$ . In other words, the wing cross section can be expressed by the conformal mapping function (continuous function) with only the angle variable,  $\theta$ , the geometry continuity can be maintained. Then the new design geometry on the new CFD grid points is generated by the inverse transformation after the definition of the angle variable  $\theta$ , which corresponds to  $x/c$  of the previous geometry CFD grids. Although the greater order  $N_c$  value can provide better reconstructed geometry, it becomes more likely that some unexpected oscillation will occur. Results of a parametric study show that the appropriate smoothing order  $N_c$  is of 15th order.

The wing geometry at each cross section should be smoothed along the span-wise direction because of the three-dimensional (3D) configuration. If a geometrical value such as  $z$  is smoothed, then the wing cross-section continuity might be lost. In this smoothing process, the coefficients of the conformal mapping function ( $P_n$ ,  $Q_n$ ) are smoothed using a polynomial equation from least squares approximation which are defined as

$$P_n(y) = \sum_{k=0}^{N_s} a_{k,n} y^k, \quad (4)$$

$$Q_n(y) = \sum_{k=0}^{N_s} b_{k,n} y^k. \quad (5)$$

At the same time, because the flat wing is used in the wing cross section smoothing as described above, the wing cross sections are retransformed to a twist wing using the twist angle  $\tau$  (deg) by the least squares approximation polynomial. The twist angle defined as

$$\tau(y) = \sum_{k=0}^{N_s} c_k y^k. \quad (6)$$

A parametric study was also conducted for order of the polynomial. Furthermore, results show that the appropriate smoothing order  $N_s$  is 12th order.

Finally, the variables for the definition of the planform such as the leading edge position and the chord length are used directly from the base-line geometry (initial geometry) to maintain the original planform including kink position discontinuity.

Cross-sections used in the shape smoothing process were increased from 14 sections to 90 sections, which are almost all sections of the result from the inverse design. In the final analysis, the term of the smoothing process was decreased drastically from 1.5 days to a few minutes by the effect of the automation system, even though the use of the cross section increases.

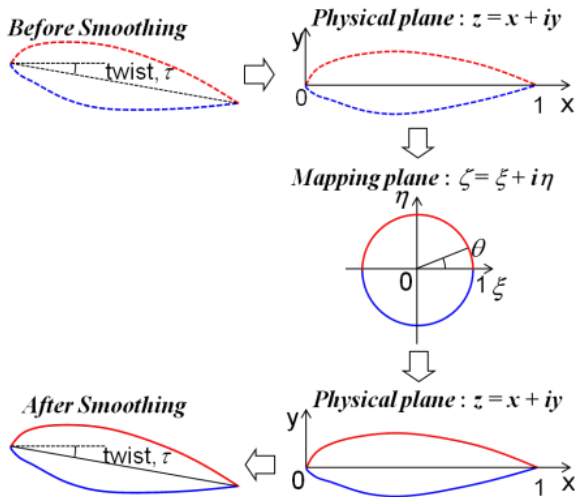


Fig 6. Smoothing image by conformal mapping [14,15].

### 3.1.3 CFD analysis method

The multi-block structured grid CFD solver called the Unified Platform for Aerospace Computation Simulation (UPACS) [16] was used in this NLF wing design process. The multi-block structured grid code (UPACS)

developed by JAXA is based on a cell-centered finite volume method in which the convection terms of the governing equations are discretized using Roe's flux difference splitting scheme with the MUSCL second-order extrapolation and vanAlbada limiter. The Matrix Free Gauss–Seidel (MFGS) implicit method is used for time integration. In this design process, the viscosity effect is considered because the wing camber is changed slightly by the displacement thickness deriving from the viscosity effect. The governing equation is the Reynolds averaged Navier–Stokes (RANS) equation with fully turbulent flow to prevent laminar separation on the wing surface. However, UPACS has some turbulence model options. This study used the Baldwin–Lomax model [17] for computation in the UPACS turbulence models to simulate turbulent flow: the lowest working load.

### 3.1.4 Inverse design method

The inverse design [10] system determines the wing section geometry, which has coordinates of  $(x, y, z)$ . The equation to express a wing surface is  $z=f(x,y)$ . The  $x$  coordinate is in the chord direction; the  $y$  coordinate is span-wise, as shown in Fig. 7. The  $z$  coordinate is in the wing thickness direction. The inverse problem of the design part is expected to handle the  $\Delta$ -value, which is the difference between the two states of a flow field. The formulation goal is to obtain the mathematical function to relate  $\Delta C_P$  to geometrical correction of wing surface  $\Delta f$ . Performing Green's theorem and calculus on the flow equation of the small perturbation approximation on a flow field for a thin wing obtained the following equations: Eqs. (7)–(12). These inverse design equations are divided into the wing thickness part and the wing camber part. In these equations,  $\beta = \sqrt{M_\infty^2 - 1}$ .

Wing thickness part:

$$\Delta w_s(x, y) = -\Delta u_s(x, y) - \frac{1}{\pi} \int_{\tau_+} \int \frac{(x - \xi) \Delta w_s(\xi, \eta)}{[(x - \xi)^2 - (y - \eta)^2]^{3/2}} d\eta d\xi, \quad (7)$$

where

$$\Delta u_s(x, y) = -\frac{1}{2\beta^2}(\Delta C p_+ + \Delta C p_-), \quad (8)$$

$$\Delta w_s(x, y) = -\frac{1}{\beta^3} \frac{\partial}{\partial x} (\Delta f_+ - \Delta f_-). \quad (9)$$

Wing camber part:

$$\begin{aligned} \Delta w_a(x, y) &= -\Delta u_a(x, y) \\ &- \frac{1}{\pi} \int_{\tau_+} \int \frac{(x-\xi)\Delta u_a(\xi, \eta)}{(y-\eta)^2 \sqrt{(x-\xi)^2 - (y-\eta)^2}} d\eta d\xi, \end{aligned} \quad (10)$$

where

$$\Delta u_a(x, y) = -\frac{1}{2\beta^2}(\Delta C p_+ - \Delta C p_-), \quad (11)$$

$$\Delta w_a(x, y) = -\frac{1}{\beta^3} \frac{\partial}{\partial x} (\Delta f_+ + \Delta f_-). \quad (12)$$

Eqs. (7) and (10) are the fundamental equations used to determine the geometrical correction. Subscript + indicates that the variable is on the upper surface of the wing, while subscript – denotes the lower surface. The area for integration, denoted by  $\tau_+$ , is the upper wing surface limited by the forwarded Mach cone from a point  $P(x, y)$  and the leading edge line.  $P$  is located at the center of every panel on the wing where the discretized equations are evaluated. The integral area  $\tau_+$  the triangular planform and  $P$  are also shown in Fig. 7. In Eqs. (7) and (10),  $\xi$  and  $\eta$  are integral variables that correspond respectively to  $x$  and  $y$  in the integration area ( $\tau_+$ ). The 3D effect is considered not only by the chord variable ( $x, \xi$ ) but also span-wise variables ( $y, \eta$ ). The computational panel for the inverse design in this study has 150 nodes along the chord direction ( $x, \xi$ ) with appropriate stretched width and 100 nodes along the span-wise direction ( $y, \eta$ ) with equal distance: 1% each. The Eq. (7) is a Volterra integral equation of the second kind for  $\Delta w_s$ . Actually,  $\Delta w_s$  is associated with the chord-wise thickness change at  $(x, y)$  on a wing. Eq. (10) is the integral expression for  $\Delta w_a$ , which is associated with the chord-wise

curvature change of the wing section camber, at  $(x, y)$ .

The unknown geometrical correction function,  $\Delta f$ , which is the  $z$  coordinate change of the wing surface, is calculated using  $\Delta w_s(x, y)$  and  $\Delta w_a(x, y)$ .

$$\begin{aligned} \Delta f_{\pm}(x, y / \beta) \\ = \frac{\beta^3}{2} \int_{L.E.}^x [\Delta w_s(\xi, y) \pm \Delta w_a(\xi, y)] d\xi. \end{aligned} \quad (13)$$

Consequently the  $z$  coordinate value on the wing surface of the next generation ( $f_{n+1}(x, y)$ ) is expressed as presented below.

$$f_{\pm, n+1}(x, y) = f_{\pm, n}(x, y) + \lambda_{n+1} \cdot \Delta f_{\pm, n+1}(x, y). \quad (14)$$

Therein,  $n$  signifies the prior design generation;  $n+1$  is the next design generation. The  $\lambda_n$  is a relaxation coefficient for the geometrical correction function. When  $\lambda_n=1.0$ , the next generation geometry fully takes in the geometrical correction  $\Delta f$ . However, the full geometrical correction sometimes induces unexpected divergent pressure distributions. In this case, the relaxation coefficient of less than 1.0 ( $\lambda_n < 1.0$ ) is applied to avoid the divergent tendency.

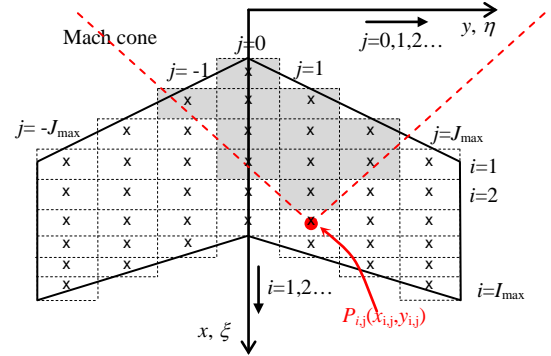


Fig 7. Coordinates and panels for formulation of the inverse problem of wing design [8,9,10].

### 3.1.5 Evaluation of the design shape

As criteria to judge the design, evaluation methods of two kinds are introduced.

The first one, which is applied to the inverse design cycle, is a quantitative criterion of the difference from the target to the current pressure distributions. The role of the inverse

design method is to obtain a wing shape that realizes the prescribed target pressure distribution. The design results are evaluated by the degree to which the resulting pressure distribution agrees with the target one. To evaluate this quantitative agreement, an objective function is defined as

$$I = \frac{\int_{y/s_{\min}}^{y/s_{\max}} \oint_{up\&low} |C_{p,design} - C_{p,target}| d(x/c)d(y/s)}{\int_{y/s_{\min}}^{y/s_{\max}} \oint_{up\&low} d(x/c)d(y/s)}, \quad (15)$$

where  $y/s_{\min}$  and  $y/s_{\max}$  indicate the design region. In the NEXST-1 airplane design process, the span-wise region is defined from  $y/s=0.12$  to  $y/s=0.9$ . In the actual inverse design process, more detailed aspects of the pressure difference should be monitored to obtain a higher performance natural laminar wing. The Eq. (15) can be transformed to obtain the breakdown objective function easily. When these objective functions drop below a sufficient level or saturate during the last few cycles, the inverse design cycle is finished.

The other criterion is to estimate how a wide NLF area is realized on a wing surface. After the inverse design cycle is finished, stability analysis [6,7] based on  $e^N$  method is performed to predict the transition location on the upper wing surface.

### 3.2 Modified design method for high- $Re$ number condition

In this study, six modifications of the design methods presented above are applied to achieve the NLF wing for a high- $Re$  number condition. Details of the six modifications are explained below.

#### 3.2.1 Relaxation of the geometrical correction

The directly used geometrical correction  $\Delta z(x,y)=\Delta f(x,y)$  causes  $C_p$  oscillation, especially around the leading edge [10]. This  $C_p$  oscillation grows divergently with every design cycle. Furthermore, results show that relaxation of the geometrical correction is efficient to suppress  $C_p$  oscillation. The relaxation coefficient,  $\lambda(x,y)$  for the geometrical correction is applied to Eq. (14). Figure 8 presents  $C_p$  distributions of an

investigation of the effect of the relaxation coefficient. It shows the  $C_p$  distribution history of the NEXST-1 design at  $x/c=0.5$ . Some oscillations are observed around the leading edge in the case of  $\lambda=1.0$ . However, the  $C_p$  distributions in the case of  $\lambda=0.5$  are more stable. The results indicate that the relaxation of the geometrical correction is effective to obtain the stable  $C_p$  distributions.

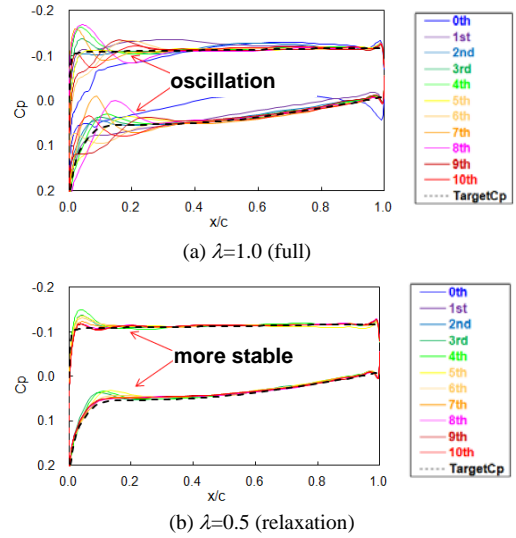


**Fig 8.  $C_p$  distribution history with and without relaxation**

#### 3.2.2 Reduction of terms of the inverse design equation

The inverse design equation is modified in order to obtain the designed configuration more stable. In the right hand side of the Eqs.(7) and (10), the first term and the second term represent 2-dimensional effect and the 3-dimensional effect for the geometrical correction respectively. The 3-dimensional effect term, especially for the wing camber part (Eqs.(10)), occurs an unexpected numerical oscillation along the span direction in case of the narrow span-wise panel in the inverse design optimizer. To avoid the numerical oscillation, the selectable option (the 2-dimensional or 3-dimensional) for the inverse design method is used in this study. The 2-dimensional inverse design means that only the first term in the right hand side of the Eqs.(7) and (10) is applied to the inverse design optimizer. Therefore, the geometrical correction function(Eqs.(13)) can be simplified to Eqs.(16).

$$\Delta f_{\pm}(x, y/\beta) = \frac{\beta}{2} \int_{L.E.}^x \Delta C_{p,\pm}(\xi, y) d\xi. \quad (16)$$

In this study, the 3D inverse design equation (Eq. (10)) is used for the low- $Re$  number condition. The 2D inverse design equation (Eq. (16)) is used for the high- $Re$  number condition.

### 3.2.3 Reduction smoothing strength through design cycles

Overly weak smoothing of the designed airfoil at the beginning of the design cycle also causes unexpected  $C_p$  oscillation. At the first design cycle,  $N_c=4$  of Eq. (3) is used for smoothing by a conformal mapping function. Then the smoothing strength weakens step-by-step with design cycles. Finally,  $N_c=50$  is applied at the final design cycle. Effects of this modification have already been found using the same design system for the other configuration.

### 3.2.4 Modification of the T.E. closing method

The inverse designed airfoil immediately after the optimizing process has an open trailing edge or a crossed trailing edge, as shown in Fig. 9, because the geometrical corrections of the upper wing and the lower wing are calculated independently in the inverse design method. Basically, for an NLF wing design of the upper wing surface, the lower wing surface is rotated around the leading edge to close to the trailing edge. Deformation near the lower leading edge is less than the deformation of the trailing edge. However, the rapid pressure gradient from the stagnation point to the leading edge is important because the target pressure distribution of the high- $Re$  number condition has a rapid increased pressure gradient, as shown in Fig. 4. It is desirable to keep the designed airfoil shape around the leading edge not only on the upper surface but also on the lower surface. The new approach is to preserve the airfoil shape from the leading edge to the  $x/c=0.5$  of the lower surface in the trailing edge closing phase immediately after the inverse design. The upper airfoil surface is also retained. Furthermore, then, the lower surface backward from  $x/c=0.5$  is connected smoothly to the trailing edge of the

upper surface, as shown in Fig. 9(b). Therefore, the geometrical correction by the inverse design method is used almost directly, except the lower and backward region of the airfoil.

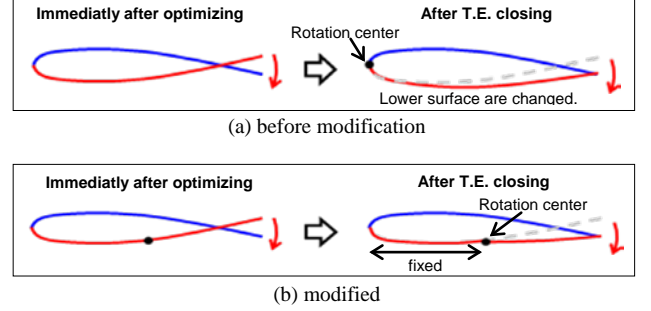


Fig 9. T.E. closing image.

### 3.2.5 Starting from the target $C_p$ of the low- $Re$ number condition

In the high- $Re$  number condition, the NLF design becomes difficult because of its pressure gradient at the leading edge of the target  $C_p$ . In this study, a multi-target inverse design method is proposed to solve the high- $Re$  number problem. The target  $C_p$  of the low- $Re$  number condition, which has a shallower pressure gradient at the leading edge than the high- $Re$  number as shown in Fig. 10, is used at the beginning of the design cycles until saturation. Then, the next NLF design cycles are performed using the high- $Re$  number target  $C_p$ . Details of the effectiveness are described below.

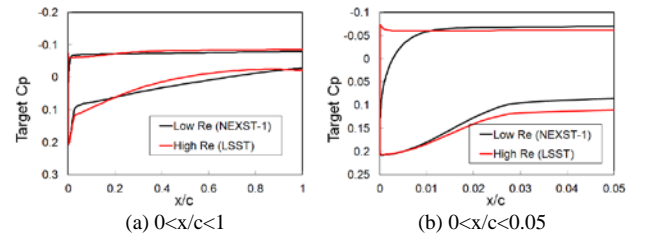


Fig 10. Target  $C_p$  at  $y/s=0.3$  (Low- $Re$  vs. High- $Re$ ).

### 3.2.6 Eliminate the geometrical correction of the lower surface

If the geometrical correction of the lower surface is greater than that of the upper surface, then the lower surface affects the upper surface after the smoothing process in spite of the independent geometrical correction by the optimizer between the upper surface and the lower surface. In this study, the geometrical correction of the lower surface is eliminated by replacement of the target  $C_p$  to the former

designed  $C_p$  distribution from the CFD results to examine the geometrical correction of the upper surface specifically. Therefore, it can be concentrated to the NLF design of the upper surface.

## 4 Results and discussion

### 4.1 Overview of the NLF design

Table 1 presents an overview of the NLF design method of each modification as described above. The circle in Table 1 shows that the modification is applied. The cross in Table 1 shows non-modification. In the NEXST-1 (low- $Re$  condition), the design process related to the geometry (Mod. 2, 3 and 6) has been manually conducted and modified. However, in the LSST (high- $Re$  condition), the automatic design process is applied to the design process related to the geometry. Case A is the first trial design case. Case B is the latest design case.

The modification Mod. 1 and Mod. 2 are applied to both of the high- $Re$  design (Case A and Case B). The effect of the Mod. No. 1 was described in an earlier report [10]. The relaxation coefficient  $\lambda(x/c)$  of the Eq. (14) is defined as presented below.

$$\lambda(x/c) = \begin{cases} 0.5 & (x/c = 0) \\ 1.0 & (x/c = 1) \end{cases} \quad (17)$$

In that equation, the relaxation coefficient  $\lambda(x/c)$  is connected smoothly from the leading edge ( $x/c = 0$ ) to the trailing edge ( $x/c = 1$ ) by a hyperbolic tangent function.

Figure 11 shows the smoothing order ( $N_c$ ) of the Eq. (3) of each design cycle. The constant smoothing order,  $N_c=15$  is used for Case A. The Case A was stop at the 4th design cycle because the obtained  $C_p$  distributions seemed to be

saturated. The smoothing order  $N_c$  is increased step-by-step through the design cycle of Case B. However, the  $N_c=4$  is used at the first design cycle of the Case B. Subsequently, the smoothing order is increased to the  $N_c=15$ . Then the smoothing order is increased again if saturation is observed with the results of the designed  $C_p$  distributions. This rule applies to the whole design cycle for Case B (Mod. 3). Finally, the smoothing order becomes  $N_c=50$  at the latest design.

The most important modification of Case B is the starting from the target  $C_p$  of the low- $Re$  number condition (Mod. 5). In this study, the baseline configuration is used from the NEXST-1 configuration, which is designed on the condition of the low- $Re$  number. The high- $Re$  number airplane, called LSST, represents an actual supersonic airplane with 91.4 m length as shown in Fig. 2. The wing planform, lift coefficient  $C_L = 0.1$  and Mach number  $M=2.0$  correspond to the NEXST-1 airplane. Altitude  $H=18$  km and  $Re$  number based on MAC  $Re_{MAC}=126 \times 10^6$  differ from those of NEXST-1.

Modification of the trailing edge closing method (Mod. 4) and elimination of the geometrical correction of the lower surface (Mod. 6) are applied to the Case B to examine the upper surface NLF design specifically.

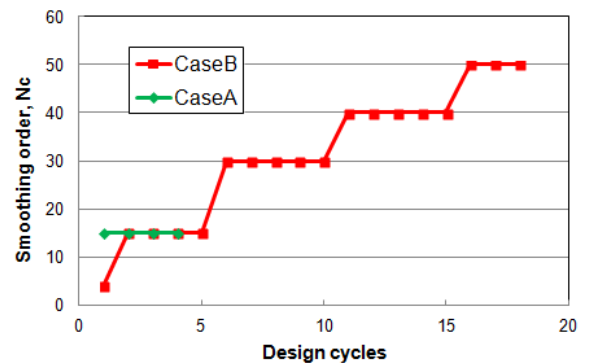


Fig 11. Smoothing order during the design cycles.

Table 1. Design overview

No.	Modified design method	Low Re	High Re (LSST)	
		(NEXST-1)	CaseA	CaseB
Mod. 1	Relaxation of the geometrical correction	manually	o	o
Mod. 2	Reduction of term of the inverse design equation	x (3D)	o (2D)	o (2D)
Mod. 3	Reduction smoothing strength through design cycles	manually	x	o
Mod. 4	Modification of the T.E. closing method	manually	x	o
Mod. 5	Starting from the target $C_p$ of the low Re number condition	x	x	o
Mod. 6	Eliminate the geometrical correction of the lower surface	x	x	o

### 4.2 Pressure distributions and airfoils

Figure 12 presents a comparison of the  $C_p$  distributions on the designed wing surface. Case A shows oscillation around the leading edge of the upper surface. This oscillation and the suction peak are suppressed in Case B on all cross sections. Moreover, Case B is close to the target  $C_p$  distributions. Some discrepancies are apparent on the lower surface around the aft wing, which results from focusing of the upper surface design method. After a sufficient upper surface pressure distribution for NLF wing is obtained using this design method, the lower surface might be designed with a fixed upper surface geometry. The same tendencies are observed also from the enclosed  $C_p$  distribution, as presented in Fig. 13. Results show that the modification for the inverse design method is effective for the supersonic NLF design on the high- $Re$  number condition.

Figure 14 presents the designed airfoils. The designed airfoil at in-board section ( $y/s=0.3$ ) has a larger twist angle than the baseline configuration and the drooped leading edge. Furthermore, the designed airfoil at the out-board section ( $y/s=0.7$ ) has less of a twist angle than the baseline configuration has. The lower surface geometry should be deformed to a realistic airfoil after the upper surface design.

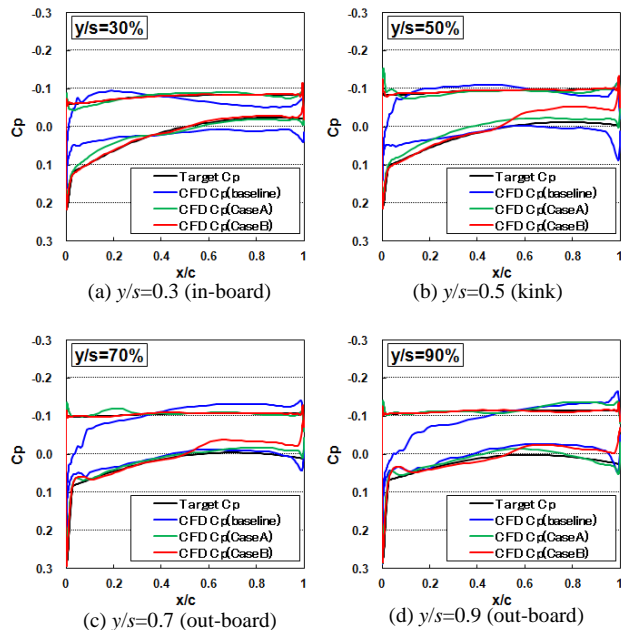


Fig 12.  $C_p$  distribution on the wing surface.

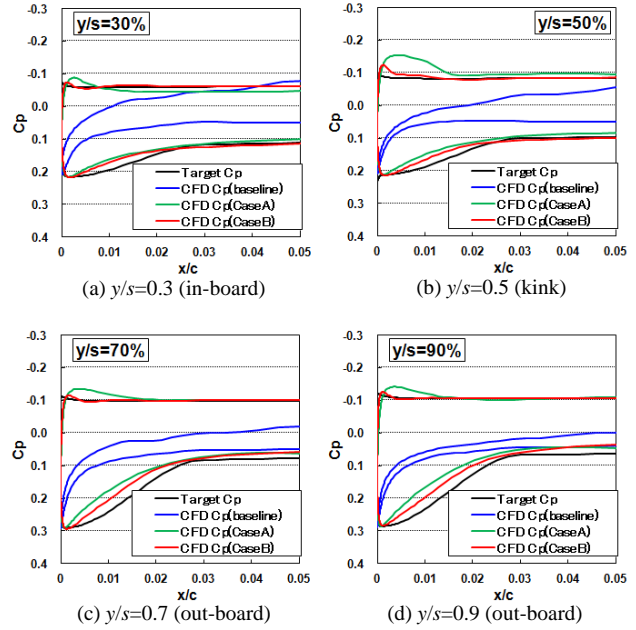


Fig 13. Enclosed  $C_p$  distribution around the L.E.

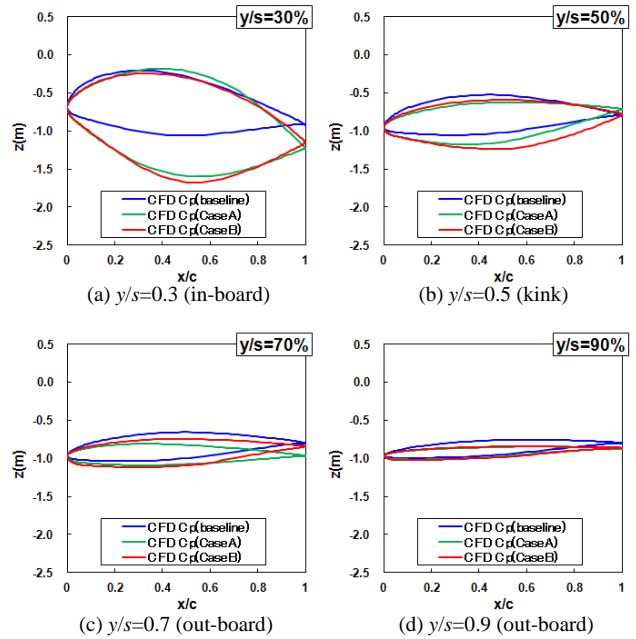


Fig 14. Designed airfoils.

### 4.3 Histroy of the design cycles

Figure 15 shows the breakdown history of the objective function from Eq. 15 of the Case B on the upper surface. The objective function decreases rapidly until the third design. Then the objective function value gradually decreases while repeating decrease and saturation. This change seems to be related with the smoothing order  $N_c$  (Fig.11). Finally, the Case B was

stopped at the 18th design cycle because the saturation is observed in this objective function and the designed  $C_p$  distributions.

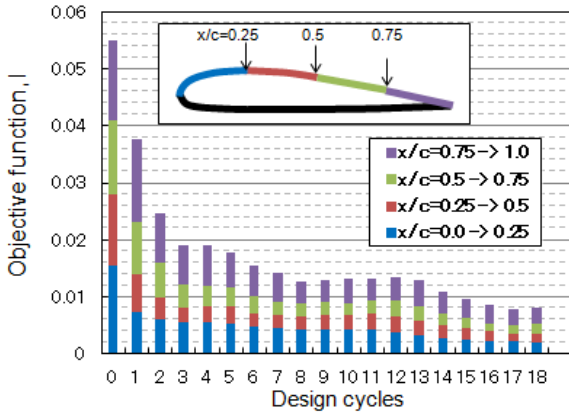


Fig 15. Breakdown history of the objective function on the upper surface (Case B).

#### 4.4 Predicted transition location

The boundary layer transition is estimated using current  $e^N$  method based on linear stability theory. Figure 16 portrays the estimated boundary layer transition location based on each  $C_p$  distribution and an assumption of judge condition of  $N=14$  at the designed  $Re$  number conditions, which corresponding to  $H=18$  km altitude. Some cross sections cannot obtain the transition location because of computational problems.

Regarding the in-board, the transition locations of the Case A are more forward than the “Target” ones and are close to the “Baseline” locations because of the  $C_p$  distribution oscillation. The boundary layer transition position of the Case B is located backward region ( $x/c=0.06-0.65$ ) ( $x_{Transition}-x_{L.E}=1.9-5.2$  m) in all span-wise direction because of the suppression of the too much suction peak around the leading edge. It is caused by the effect of the some modifications as mentioned above. The predicted laminar flow region by the modified design method was improved compared with the previous design results. It is close to the target laminar flow region. Table 2 presents the laminar flow area to the whole area ratio on the upper surface by the predicted boundary layer transition location. The baseline configuration has almost turbulent flow. The Case B has 22.1%

laminar region on the upper surface. Therefore, results suggest that the modified NLF design method with inverse design based on CFD analysis is applicable to the higher  $Re$  number of supersonic transports.

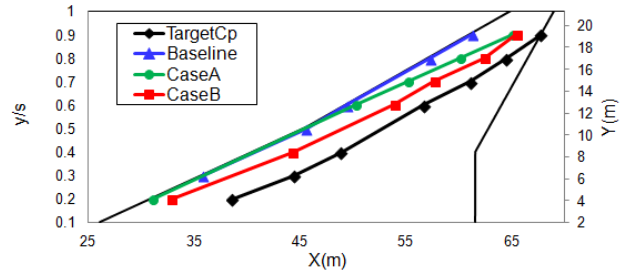


Fig 16. Predicted transition location of the design configuration.

Table 2. Laminar area

	Target	Baseline	Case A	Case B
$S_{lam}/S_{all}$ (upper surface)	43.5%	0.6%	6.6%	22.1%

#### 5 Conclusion

The supersonic NLF wing design method was modified and applied to a high- $Re$  number supersonic transport. Relaxation of the geometrical correction and the variable smoothing strength can suppress an unexpected oscillation of the pressure distribution, especially around the leading edge. Results show that the multi-target pressure inverse design method, which started from using low- $Re$  number target pressure and which changed to the using high- $Re$  number target pressure after the low- $Re$  number design, is effective for the NLF wing design on the high- $Re$  number supersonic condition. The designed pressure distribution on the wing surface with some modification has a rapid pressure gradient around the leading edge. It is close to the target pressure distributions. The predicted laminar flow region by the modified design method was improved compared with the previous design results. It is close to the target laminar flow region. Therefore, results suggest that the modified NLF design method with inverse design based on CFD analysis is applicable to the higher  $Re$  number of supersonic transports.

## Acknowledgments

The authors would like to acknowledge Prof. K. Matsushima for her valuable advice and providing the inverse design optimizer. And they also thank Mr. K. Ito for his support of the analysis about the NLF design.

## References

- [1] Ohnuki T, Hirako K and Sakata K. National Experimental Supersonic Transport Project. *Proceedings of International Congress of the Aeronautical Science*, 2006-1.4.1, Sep. 2006.
- [2] Ishikawa H, Kwak D.-Y and Yoshida K. Numerical Analysis on Flight-Test Results of Supersonic Experimental Airplane NEXST-1. *AIAA Journal of Aircraft*, Vol.45, No.5, 2008, pp. 1505-1513.
- [3] Kuchemann D. *The Aerodynamic Design of Aircraft*. Pergamon Press, June, 1978.
- [4] Carlson H.W and Miller D.S. Numerical Method for the Design and Analysis of Wings at Supersonic Speed. *NASA TN D-7713*, 1974.
- [5] Ashley H and Landahl M. *Aerodynamics of Wings and Bodies*. Dover Publications Inc., 1965.
- [6] Yoshida K, Iwamiya T, Ueda Y and Ishikawa H. Boundary layer transition analysis of the scaled supersonic experimental airplane. *NAL's 2nd SST-CFD Workshop*, 85-90, 2000.
- [7] Ueda Y, Ishikawa H and Yoshida K. Three dimensional Boundary Layer Transition Analysis in Supersonic Flow Using a Navier-Stokes Code. *Proceedings of International Congress of the Aeronautical Science*, 2004-2.8.2, Sep. 2006.
- [8] Matsushima K, Iwamiya T and Nakahashi K. Wing design for supersonic transition using integral equation method. *Engineering Analysis with Boundary Elements* 28, pp. 247-255, 2004.
- [9] Matsushima K, Sakashita S and Nakahashi K. Supersonic Wing Design Method using an Inverse Problem for Practical Application. *Proceedings of KASA-JSASS Joint International Symposium on Aerospace Engineering*, 2008.
- [10] Ishikawa H, Ohira K, Inoue Y, Matsushima K and Yoshida K. Development of Supersonic Natural Laminar Flow Wing Design System using CFD-based Inverse Method. *Proceedings of International Congress of the Aeronautical Science*, 2012-2.2.1, Sep. 2012.
- [11] Ueda Y, Yoshida K, Matsushima and Ishikawa H. Method of Designing Natural Laminar Flow Wing for Reynolds Number Equivalent to Actual Supersonic Aircraft. *U.S. Patent Application No, 13/325,742*, Docket No. 111571, 26 Jan. 2012.
- [12] Ueda Y, Yoshida K, Matsushima and Ishikawa H. Supersonic Natural-Laminar-Flow Wing-Design Concept at High-Reynolds-Number Conditions. *AIAA Journal*, Vol. 52, No. 6, pp. 1294-1306, 2014.
- [13] Joslin, R. D. Aircraft Laminar Flow Control. *Annual Review of Fluid Mechanics*, Vol. 30, Jan. 1998, pp. 1–20, 1998.
- [14] Imai I. *Conformal mappings and their applications* (in Japanese). Iwanami Shoten, Tokyo, 1979.
- [15] Squyers R. *Potential Flow Generation about Two-dimensional Airfoil Profiles Using the Isao Imai Conformal Transformation*. University of Texas at Arlington., 1980.
- [16] Takaki R, Yamamoto K, Yamane T, Enomoto S and Mukai J. The Development of the UPACS CFD Environment. *High Performance Computing, Proc. Of ISHPC 2003*, Springer, pp.307-319, 2003.
- [17] Baldwin B.S and Lomax H. Thin Layer Approximation and Algebraic Model for Separated Turbulent Flows. *AIAA 16th Aerospace Sciences Meeting*, Huntsville, Alabama, January 16-18, 1978.

## Copyright Statement

The authors confirm that they, and/or their company or organization, hold copyright on all of the original material included in this paper. The authors also confirm that they have obtained permission, from the copyright holder of any third party material included in this paper, to publish it as part of their paper. The authors confirm that they give permission, or have obtained permission from the copyright holder of this paper, for the publication and distribution of this paper as part of the ICAS 2014 proceedings or as individual off-prints from the proceedings.

## Contact Author Email Address

mail to:hiroaki@chofu.jaxa.jp